http://doi.org/10.35784/iapgos.7776 *received: 19.05.2025 | revised: 05.01.2026 | accepted: 19.01.2026 | available online: 30.03.2026*

POSITIONAL CODING METHOD IN DIFFERENTIAL WAVE SPACE

Volodymyr Barannik[1], Anatolii Berchanov[1], Valeriy Barannik[2], Dmytro Uzlov[1], Mykola Dihtiar[3], Mykhailo Osovytskyi[3], Andrii Sushko[3], Yurii Babenko[4]

[1]V.N. Karazin Kharkiv National University, Kharkiv, Ukraine, [2]Kharkiv National University of Radio Electronics, Kharkiv, Ukraine, [3]Ivan Kozhedub Kharkiv National Air Force University, Kharkiv, Ukraine, [4]Taras Shevchenko National University of Kyiv, Kyiv, Ukraine

Abstract. *The study addresses the development of intelligent services for the transmission of infrared (IR) imagery, with a focus on the generation and exploitation of semantic metadata that reflects the informativeness and spatial structure of image regions. Such metadata facilitates classification of object types and states and supports the selection of informative fragments within IR frames. These functionalities are particularly relevant in applications involving unmanned onboard systems, where tasks such as dynamic object tracking and autonomous navigation impose stringent requirements on the timeliness and fidelity of visual data. With the increasing complexity of operational scenarios, the demands for high information completeness – such as higher frame rates, improved resolution, and reduced distortion – place significant burdens on infocommunication subsystems. This induces a fundamental conflict between the need for low-latency transmission and the preservation of the structural integrity of IR data. To address this issue, the paper formulates a new scientific and applied objective: to enhance the quality of IR-based intelligent services through the design of a positional coding method in differential wave space. The proposed method operates by hierarchically segmenting IR images to localize structurally homogeneous regions, applying differential wave transformations to capture local contrast dynamics, and encoding positional information relative to wavelet-domain variations. This positional representation enables spectral-differential group coding, which effectively reduces bit volume while preserving spatial-semantic features. An experimental evaluation using the Open Turbulent Image Set (OTIS) – consisting of PNG-encoded IR images with varying levels of informativeness – demonstrated an average bit volume reduction of approximately 37%. Comparative analysis with JPEG2000 encoding of 16-bit images revealed a 25% gain in compression ratio while maintaining equivalent PSNR values.*

Keywords: speed of delivery of infrared images, spectral-wave domain, bit volume reduction, spectral group coding, semantic frame integrity, frame segmentation

METODA KODOWANIA POZYCYJNEGO W DIFERENCYJNEJ PRZESTRZENI FALOWEJ

Streszczenie. *Badanie dotyczy rozwoju inteligentnych usług w zakresie transmisji obrazów w podczerwieni (IR), ze szczególnym uwzględnieniem generowania i wykorzystania metadanych semantycznych, które odzwierciedlają informacyjność i strukturę przestrzenną obszarów obrazu. Metadane takie ułatwiają klasyfikację typów i stanów obiektów oraz wspierają wybór fragmentów zawierających informacje w ramach klatek IR. Funkcje te są szczególnie istotne w zastosowaniach związanych z bezzałogowymi systemami pokładowymi, gdzie zadania takie jak dynamiczne śledzenie obiektów i autonomiczna nawigacja nakładają surowe wymagania dotyczące aktualności i wierności danych wizualnych. Wraz ze wzrostem złożoności scenariuszy operacyjnych, wymagania dotyczące wysokiej kompletności informacji – takie jak wyższa częstotliwość klatek, lepsza rozdzielczość i mniejsze zniekształcenia – stanowią znaczne obciążenie dla podsystemów infokomunikacyjnych. Powoduje to fundamentalny konflikt między potrzebą transmisji o niskim opóźnieniu a zachowaniem integralności strukturalnej danych IR. Aby rozwiązać ten problem, w artykule sformułowano nowy cel naukowy i praktyczny: poprawa jakości inteligentnych usług opartych na IR poprzez zaprojektowanie metody kodowania pozycyjnego w przestrzeni fal różnicowych. Proponowana metoda działa poprzez hierarchiczną segmentację obrazów IR w celu zlokalizowania obszarów o jednorodnej strukturze, zastosowanie transformacji fal różnicowych w celu uchwycenia lokalnej dynamiki kontrastu oraz kodowanie informacji o położeniu względem zmian w dziedzinie falowej. Ta reprezentacja położenia umożliwia spektralno-różnicowe kodowanie grupowe, które skutecznie zmniejsza objętość bitową przy zachowaniu cech semantycznych przestrzeni. Ocena eksperymentalna z wykorzystaniem zestawu Open Turbulent Image Set (OTIS) – składającego się z obrazów IR zakodowanych w formacie PNG o różnym poziomie informacyjności – wykazała średnią redukcję objętości bitów o około 37%. Analiza porównawcza z kodowaniem JPEG2000 obrazów 16-bitowych wykazała 25% wzrost współczynnika kompresji przy zachowaniu równoważnych wartości PSNR.*

Słowa kluczowe: szybkość dostarczania obrazów w podczerwieni, dziedzina fal spektralnych, redukcja objętości bitów, kodowanie grup spektralnych, integralność ram semantycznych, segmentacja ram

Introduction

The current state of infocommunication technologies tends towards their intellectualization. This is driven by the development of the theoretical base and the performance of computing systems (hardware and technological base).

This characteristic trend also applies to technologies related to providing visual information services. Visual information includes information channels formed by the following sources: optoelectronic, infrared (thermal), radar, and television. Each of these information channels has distinctive features for its applied use. The integrated use of various types of visual information sources creates conditions for obtaining the most comprehensive and reliable information about monitoring or research objects.

Recently, practical applications indicate that the infrared channel is one of the important sources of visual information. This is due to the following characteristic factors of thermal channels:

- detection of objects that do not have radar contrast and are not detected by devices operating in the visible range of the spectrum (for example, at night);
- detection of objects camouflaged under nets, including small objects, as well as distinguishing real objects from false ones based on the difference in "object-background" emission intensity;
- revealing and identifying the presence of equipment and vehicles in areas of concentration and movement.

Accordingly, in general, it is necessary to provide an informational resource with the required level of quality attributes upon user request. In the case of intelligent information services, it becomes possible to additionally provide metadata. Metadata is generated based on the results of intelligent analysis of infrared (IR) images. The result of intelligent analysis of IR images may include [1, 2]:

- identification of image fragments based on their level of informativeness;
- identification of objects in the image;
- recognition of the class and condition of objects of interest;
- clustering and/or typification of a set of heterogeneous objects in operational areas;
- additional information as a component of overall visual monitoring.

These processes are used in the following applied tasks [3, 5]:

- detection of objects of interest during remote monitoring;
- creation of databases of thermal profiles of targets;
- predicting the behavioral dynamics of objects;
- semantic search for objects of interest in IRI databases;
- selective protection of infrared image fragments;
- positioning of dynamic objects and tracking them with the ability to map their location.
- autonomous guidance (self-guidance) of robotic on-board systems relative to objects of interest;
- artificial vision systems.

In turn, users of infrared technology can include:

- a decision-making person;
- information systems (machine complexes).

Currently, automated and autonomous modes are used depending on the class of applied tasks. A relevant and significant example here is the solution of applied tasks using on-board systems [1, 3, 5].

Most often, onboard systems are used for:

- obtaining information regarding remote monitoring (control) areas;
- remote detection, classification, and analysis of objects of interest;
- detection and tracking of dynamic objects.

Then, along with the speed of delivery of IRI, it is important to ensure the required level of their completeness, integrity and relevance. Therefore, requirements for the following increase:

- increasing the number of updated frames of the IR image resource that are generated and transmitted per unit of time;
- limiting the distortions introduced during the processing of IR images;
- increasing the number of pixels used to describe monitoring objects.

This results in a significant increase in the informational load on infocommunication systems regarding data processing and transmission.

Thus, there is a contradiction between the requirements for quality characteristics, namely:

- the timeliness of delivering the stream of IR images and the corresponding need for their compact representation;
- the integrity of IR images and the corresponding limitations on the use of processing technologies, which are associated with the introduction of distortions.

Therefore, a relevant ***scientific and applied task*** is to enhance the quality characteristics of providing intelligent information services based on IR sources in applied tasks using onboard systems.

Currently, technologies for image processing with elements of intelligent analysis are being developed and applied to solve such tasks. These include: JPEG2000, PNG. The main directions of technological developments in this area are as follows: [7–19, 21, 27]:

1. localization of homogeneous areas within the frame;
2. application of a model for describing impulse information, which can generally be used to separate the noise component from the information of small objects;
3. determination of object classes and their group description in IR images;
4. use of a package of typical objects and technologies for their detection in frames;
5. technologies for interpolative description of background areas in IR images.

At the same time, such technological mechanisms are [20, 22, 23]:

1. complex from the perspective of computational implementation;
2. low-effective in the case of processing IR images: with atypical content, such as in the case of preliminary monitoring of operational areas with a high level of saturation of a priori undefined objects; with a complex topology of the mutual arrangement of a large number of heterogeneous objects;
3. and those accompanied by distortions that lead to the exclusion of the possibility of reverse recovery of the semantic components of the frames.

Therefore, in modern technologies for encoding IR images, it is necessary to use methods for encoding pre-intellectually localized fragments of infrared images with the property of further increasing the level of compression of local fragments of frames while maintaining the required level of their integrity.

Thus, **the goal of the research** presented in the article is to develop a method for group coding of data in the spectral-wave space.

1. Development a positional coding method in differential wave space

To reduce the bit volume, it is proposed to use coding that will allow homogeneous segments of the image to be represented with spectral-group codes.

Homogeneity refers to the degree of correlation between neighboring pixels in an image. Therefore, the coding of such correlated pixels in the form of segments makes it possible to represent them in a smaller bit volume.

Spectral-group codes will be formed as a result of encoding groups of values from the spectral domain of the image. As a result of replacing the area with one code, the bit volume of the segment will be reduced.

Let's consider the input IR image as a two-dimensional matrix $I^{(X,Y)}$. Then $I^{(X,Y)}$ is a segment of size 8 by 8 values, where (x, y) represent coordinates of the segment. For better localization of homogeneous areas of the image, it is proposed to divide the segment $I^{(X,Y)}$ onto four mini-segments $I_{m,n}^{(x,y)}$ of size 4 by 4, where (m, n) are coordinates of the mini-segment inside the segment $I^{(X,Y)}$. In turn, the value from the mini-segment $I_{m,n}^{(x,y)}$ is addressed as $I_{m,n}^{(x,y)}(r,k)$, where (r, k) are coordinates of the value in the mini-segment $I_{m,n}^{(x,y)}$. The described hierarchy of segments can be represented by the diagram in Fig. 1.

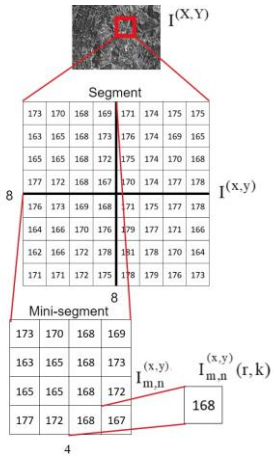

Fig. 1. Scheme of image segmentation

To reduce the range of values, we take into account the correlation dependence of the elements $I_{m,n}^{(x,y)}(r,k)$ in the mini-segment $I_{m,n}^{(x,y)}$. Let's convert the mini-segments into a difference space. For this, it is necessary to define the minimum element in the mini-segment $\alpha_{m,n}^{(x,y)}$.

$$\alpha_{m,n}^{(x,y)} = \min_{I_{m,n}^{(x,y)}(r,k) \in I_{m,n}^{(x,y)}} \{ I_{m,n}^{(x,y)}(r,k) \} \quad (1)$$

Let's transform the elements of the mini-segment $I_{m,n}^{(x,y)}$ into a difference space $I'^{(x,y)}_{m,n}$ using the following formula:

$$I'^{(x,y)}_{m,n}(r,k) = I_{m,n}^{(x,y)}(r,k) - \alpha_{m,n}^{(x,y)} \quad (2)$$

where: $I_{m,n}^{(x,y)}(r,k)$ is a value from the mini-segment, where r, k are coordinates in the mini-segment, $I'^{(x,y)}_{m,n}(r,k)$ is received a difference value element.

Considering that $I_{m,n}^{(x,y)}(r,k) \in I_{m,n}^{(x,y)}$ form a mini-segment in the difference space from the obtained elements:

$$I_{m,n}^{(x,y)}(r,k) \in I_{m,n}^{(x,y)} \Rightarrow I'^{(x,y)}_{m,n} = \{ I'^{(x,y)}_{m,n}(q,s) \} \quad (3)$$

where $I'^{(x,y)}_{m,n}$ is a mini-segment in the difference space.

Due to difference coding, excess energy between the minimum element in the mini segment $\alpha_{m,n}^{(x,y)}$ and 0 is eliminated. However, there remains a spatial redundancy that also needs to be eliminated.

To do this, it is proposed to transform the difference mini-segment $I'^{(x,y)}_{m,n}$ from the spatial domain to the time-spectral domain. This can be achieved by various methods, but the Haar wavelet transform will be used [24–26]. It has a number of advantages:

1. Low computational complexity allows data to be encoded and decoded with lower time delays.
2. Local properties, in contrast to integral ones, as in the discrete cosine transformation, allow the spectrum to be presented at low and high frequencies. Using that, additional correlation dependencies can be taken into account.

Let's represent the application of the Haar wavelet transform as a functional HT:

$$HT(I'^{(x,y)}_{m,n}) = \{ HS^{(x,y)}_{m,n}(L), HD^{(x,y)}_{m,n} \} \quad (4)$$

where: $I'^{(x,y)}_{m,n}$ is the difference mini-segment to which HT is applied; $HD^{(x,y)}_{m,n}$ is the group of high-frequency values that is calculated based on half differences; $HS^{(x,y)}_{m,n}(L)$ is the latest low-frequency value that is calculated based on half sums.

The low-frequency values $HS^{(x,y)}_{m,n}(L)$ and high-frequency $HD^{(x,y)}_{m,n}$ significantly differ between each other. More precisely the values $HD^{(x,y)}_{m,n}$ are lesser than $HS^{(x,y)}_{m,n}(L)$. This is justified by the fact that high-frequency values have detailing properties and are obtained as a result of half-difference operations. And low-frequency values are obtained as a result of half-sums. Accordingly, the dynamic range is greater for low-frequency values $HS^{(x,y)}_{m,n}(L)$ than for high-frequency values $HD^{(x,y)}_{m,n}$.

The difference in low-frequency values $HS^{(x,y)}_{m,n}(L)$ is illustrated in the histogram (Fig. 3), built on the basis of the data obtained after applying the Haar wavelet to the difference mini-segment.

The histogram shows the dynamic range of low and high frequencies:

- columns H1...H15 correspond to the module of high-frequency values $|HD^{(x,y)}_{m,n}|$;
- column L16 corresponds to the low-frequency value $HS^{(x,y)}_{m,n}(L)$.

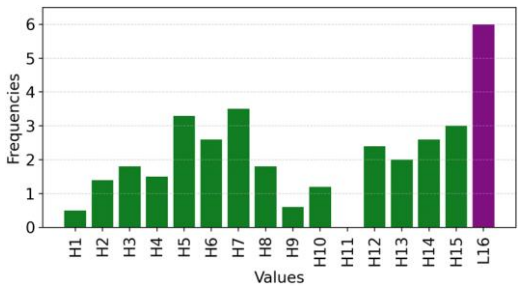

Fig. 2. Diagram of the dependence of low and high frequencies

In the given histogram, the low-frequency value $HS^{(x,y)}_{m,n}(L)$ much more than the maximum high frequency $|HD^{(x,y)}_{m,n}|$.

This significant difference must be taken into account, as it can affect the efficiency of subsequent encoding. Accordingly, coding must be performed with consideration of frequencies dynamic ranges. To do this, we will separate the low-frequency values $HS^{(x,y)}_{m,n}(L)$ into the separate group $HS^{(x,y)}$ corresponding to the segment $I^{(x,y)}$. As result the segment $I^{(x,y)}$ will be represented by a group of latest low-frequency values $HS^{(x,y)}$ and groups of high-frequency values $HD^{(x,y)}_{m,n}$.

To decode the difference mini-segment $I'^{(x,y)}_{m,n}$ among the low frequencies, only the final low-frequency value is necessary $HS^{(x,y)}_{m,n}(L)$. Therefore, the formation of a group of low-frequency values $HS^{(x,y)}$ for a segment includes only the final low-frequency values:

$$HS^{(x,y)} = \{ HS^{(x,y)}_{1,1}(L), HS^{(x,y)}_{1,2}(L), HS^{(x,y)}_{2,1}(L), HS^{(x,y)}_{2,2}(L) \} \quad (5)$$

Groups of low-frequency values $HS^{(x,y)}$ and high-frequency values $HD^{(x,y)}_{m,n}$ from the each segment $I^{(x,y)}$ need to be transformed into a more compact form. That is, to reduce their bit volume.

For that group of low-frequency values $HS^{(x,y)}$ of the segment $I^{(x,y)}$, is proposed to code using the following formula of spectral-group coding:

$$GC(HS^{(x,y)}) = \sum_{g=1}^{len(HS^{(x,y)})} floor(HS^{(x,y)}(g)) \cdot floor(\beta)^{len(HS^{(x,y)})-g}$$

$$\beta = \max_{HS^{(x,y)}(g) \in HS^{(x,y)}} \{HS^{(x,y)}(g)\} \quad (6)$$

where: β is the maximum element in the group of low-frequency values $HS^{(x,y)}$; $HS^{(x,y)}(g)$ is an element from the group of low-frequency values $HS^{(x,y)}$ with serial number g; $len(HS^{(x,y)})$ is the number of elements in the group of low-frequency values $HS^{(x,y)}$. Corresponds to the number of mini-segments in a segment $I^{(x,y)}$; $GC(HS^{(x,y)})$ is a group code from a set of low-frequency values $HS^{(x,y)}$.

In a similar way, we will apply spectral-group coding to each group of high-frequency values $HD^{(x,y)}_{m,n}$ from each mini-segment $I^{(x,y)}_{m,n}$ according to the following formula:

$$GC(HD^{(x,y)}_{m,n}) = \sum_{g=1}^{len(HD^{(x,y)}_{m,n})} floor(|HD^{(x,y)}_{m,n}(g)|) \cdot floor(\delta)^{len(HD^{(x,y)}_{m,n})-g};$$

$$\delta = \max_{HD^{(x,y)}_{m,n}(g) \in HD^{(x,y)}_{m,n}} \{|HD^{(x,y)}_{m,n}(g)|\}$$

$$len(HD^{(x,y)}_{m,n}) = M \cdot N - 1 \quad (7)$$

where: δ is the maximum element in the set of high-frequency values $HD^{(x,y)}_{m,n}$ modulo; $HD^{(x,y)}_{m,n}(g)$ is an element in the set of high-frequency values $HD^{(x,y)}_{m,n}$ with the ordinal number g; $len(HD^{(x,y)}_{m,n})$ is the number of elements in the group of high-frequency values $HD^{(x,y)}_{m,n}$ of mini-segment $I^{(x,y)}_{m,n}$; $GC(HD^{(x,y)}_{m,n})$ is a group code from a set of values $HD^{(x,y)}_{m,n}$.

The above formulas use an operation floor to separate the integer from the remainder. For example floor(4.75) = 4. Saving the remainder for lossless data recovery will be considered separately.

As a result of coding, each segment $I^{(x,y)}$ will be represented by a low-frequency code of values $GC(HS^{(x,y)})$ and codes of high-frequency values $GC(HD^{(x,y)}_{m,n})$ according to each mini-segment $I^{(x,y)}_{m,n}$.

The selection of the $I^{(x,y)}$ 8×8 segment and $I_{m,n}^{(x,y)}$ 4×4 mini-segment structure in the proposed coding method is driven by the need to balance spatial correlation modeling. An 8×8 segment provides a sufficiently large spatial context to exploit inter-pixel correlation while keeping the number of Haar-transform calls and memory accesses low, thereby minimizing algorithmic overhead. Within each segment, the use of 4×4 mini-segments enables more precise localization of homogeneous regions and allows the differential transformation to operate on smaller, structurally coherent units. This reduces the dynamic range of values prior to wavelet conversion, decreases energy in high-frequency components, and improves the effectiveness of spectral-group coding. The hierarchical decomposition thus represents an optimal compromise. Alternative block sizes were considered. However, 2×2 regions are too small to justify the transform and grouping overhead, and 16×16 regions violate the local homogeneity assumption, degrading spectral grouping performance. Smaller blocks offer finer structural adaptation but introduce excessive processing overhead, while larger blocks yield lower overhead but fail to model local variations adequately, resulting in reduced compression efficiency.

For images whose dimensions are not divisible by the segment size, border areas are completed using edge replication, where the last row and column are repeated to fill the final segments. This follows the boundary-handling strategy used in standard block-based codecs such as JPEG. The padding is internal to the encoder and removed after decoding.

Adaptive block sizes could potentially enhance content-driven localization, such mechanisms increase computational complexity and are therefore reserved for future research.

Key introduced and used mathematical expressions are described in the Table 1.

Table 1. Key expressions description

Expression	Description
$I^{(x,y)}$	Segment of size 8 by 8 values, where (x, y) represent coordinates of the segment.
$I_{m,n}^{(x,y)}$	Mini-segments of size 4 by 4, where (m, n) are coordinates inside the segment $I^{(x,y)}$.
$I_{m,n}^{(x,y)}(r,k)$	Pixel value from the mini-segment $I_{m,n}^{(x,y)}$, where (r, k) are coordinates of the value.
$\alpha_{m,n}^{(x,y)}$	Minimum element in the mini-segment.
$I'^{(x,y)}_{m,n}$	Difference space mini-segment.
$HT(I^{(x,y)}_{m,n})$	Haar wavelet transform.
$HD^{(x,y)}_{m,n}$	Group of high-frequency values.
$HS^{(x,y)}_{m,n}(L)$	Latest low-frequency value.
$HS^{(x,y)}$	Group of low-frequency values.
$GC(HS^{(x,y)})$	Group code from a set of values $GC(HS^{(x,y)})$.
$GC(HD^{(x,y)}_{m,n})$	Group code from a set of values $HD^{(x,y)}_{m,n}$.

2. Example application of the developed method

Consider image segmentation using examples. Let's take a matrix as a segment:

$$I^{(1,1)} = \begin{matrix} 173 & 170 & 168 & 169 & 171 & 174 & 175 & 175 \\ 163 & 165 & 168 & 173 & 176 & 174 & 169 & 165 \\ 165 & 165 & 168 & 172 & 175 & 174 & 170 & 167 \\ 177 & 172 & 168 & 167 & 170 & 174 & 177 & 178 \\ 176 & 173 & 169 & 168 & 171 & 175 & 177 & 178 \\ 164 & 166 & 170 & 176 & 179 & 177 & 171 & 166 \\ 162 & 166 & 172 & 178 & 181 & 178 & 170 & 164 \\ 171 & 171 & 172 & 175 & 178 & 179 & 176 & 173 \end{matrix} \quad (8)$$

Accordingly, in the role of a mini-segment $I_{1,1}^{(1,1)}$ will be the following matrix:

$$I_{1,1}^{(1,1)} = \begin{matrix} 173 & 170 & 168 & 169 \\ 163 & 165 & 168 & 173 \\ 165 & 165 & 168 & 172 \\ 177 & 172 & 168 & 167 \end{matrix} \quad (9)$$

Values from the mini-segment $A_{1,1}^{(1,1)}$ can be obtained as follows:

$$I_{1,1}^{(1,1)}(1,1)=173;\ I_{1,1}^{(1,1)}(2,1)=170$$

$$I_{1,1}^{(1,1)}(1,2)=163;\ I_{1,1}^{(1,1)}(2,2)=165$$

Let's consider an example of conversion into the difference space of a mini-segment $I_{1,1}^{(1,1)}$, formula (9). The minimum value of the mini-segment $I_{1,1}^{(1,1)}$ is $\alpha_{1,1}^{(1,1)}(1,1)=163$.

A mini-segment in the difference space $A'^{(1,1)}_{1,1}$ is formed from the generated difference values (Fig. 3).

$$I_{1,1}^{(1,1)} = \begin{matrix} 173 & 170 & 168 & 169 \\ 163 & 165 & 168 & 173 \\ 165 & 165 & 168 & 172 \\ 177 & 172 & 168 & 167 \end{matrix} \Rightarrow I'^{(1,1)}_{1,1} = \begin{matrix} 10 & 7 & 0 & 1 \\ 0 & 2 & 0 & 5 \\ 0 & 0 & 1 & 5 \\ 12 & 7 & 1 & 0 \end{matrix}$$

Fig. 3. Scheme of a difference mini-segment $I'^{(1,1)}_{1,1}$ creation

The next step is to convert the difference mini-segment $I'^{(1,1)}_{1,1}$ into the spectral domain using the Haar wavelet transform: $HT(I'^{(1,1)}_{1,1})$. Initial group of low-frequency values HS_0 is equal to the mini-segment values:

$$I'^{(1,1)}_{1,1} = HS_0 = \begin{matrix} 10 & 7 & 0 & 1 \\ 0 & 2 & 0 & 5 \\ 0 & 0 & 1 & 5 \\ 12 & 7 & 1 & 0 \end{matrix} \quad (10)$$

Calculation of a group of values HS_1 is performed as follows:

$$\begin{aligned} HS_1 = \{ & \\ \ell_1^{(1)} &= \frac{L_0(1)+L_0(2)}{2} = \frac{10+7}{2} = 8.5; \\ \ell_2^{(1)} &= \frac{L_0(3)+L_0(4)}{2} = \frac{5+6}{2} = 5.5; \\ \ell_3^{(1)} &= \frac{L_0(5)+L_0(6)}{2} = \frac{0+2}{2} = 2; \\ \ell_4^{(1)} &= \frac{L_0(7)+L_0(8)}{2} = \frac{5+10}{2} = 7.5; \\ \ell_5^{(1)} &= \frac{L_0(9)+L_0(10)}{2} = \frac{2+2}{2} = 2; \\ \ell_6^{(1)} &= \frac{L_0(11)+L_0(12)}{2} = \frac{5+9}{2} = 7; \\ \ell_7^{(1)} &= \frac{L_0(13)+L_0(14)}{2} = \frac{14+9}{2} = 11.5; \\ \ell_8^{(1)} &= \frac{L_0(15)+L_0(16)}{2} = \frac{5+4}{2} = 4.5; \\ \} &= \{\ 8.5;\ 5.5;\ 1;\ 7.5;\ 2;\ 7;\ 11.5;\ 4.5\ \} \end{aligned} \quad (11)$$

And the calculation of a group of values HD_1:

$$\begin{aligned} H_1 = \{ \\ h_1^{(1)} &= \frac{L_0(2)-L_0(1)}{2} = \frac{7-10}{2} = -1.5; \\ h_2^{(1)} &= \frac{L_0(4)-L_0(3)}{2} = \frac{6-5}{2} = 0.5; \\ h_3^{(1)} &= \frac{L_0(6)-L_0(5)}{2} = \frac{2-0}{2} = 1; \\ h_4^{(1)} &= \frac{L_0(8)-L_0(7)}{2} = \frac{10-5}{2} = 2.5; \\ h_5^{(1)} &= \frac{L_0(10)-L_0(9)}{2} = \frac{2-2}{2} = 0; \\ h_6^{(1)} &= \frac{L_0(12)-L_0(11)}{2} = \frac{9-5}{2} = 2; \\ h_7^{(1)} &= \frac{L_0(14)-L_0(13)}{2} = \frac{9-14}{2} = -2.5; \\ h_8^{(1)} &= \frac{L_0(16)-L_0(15)}{2} = \frac{4-5}{2} = -0.5; \\ \} = \{ & -1.5;\ 0.5;\ 1;\ 2.5;\ 0;\ 2;\ -2.5;\ -0.5 \} \end{aligned} \tag{12}$$

Having received the values HS_1 and HD_1 we can proceed to the next iteration, when i = 2. It consists in calculation HS_2 and HD_1 based on the obtained low-frequency values HS_1. In this way, the calculation of half-sums (11) and half-differences (12) should be repeated until the final low-frequency value is obtained.

The result of applying the Haar wavelet to the difference mini-segment $I'^{(1,1)}_{1,1}$:

$$HT(I'^{(1,1)}_{1,1}) = \begin{cases} HS^{(1,1)}_{1,1}(L) = 3.1875; \\ HD^{(1,1)}_{1,1} = \{ \\ 0.3125;\ -1.375;\ 1.75;\ -1.5; \\ 3.25;\ 2.5;\ -3.5;\ -1.5;\ 0.5; \\ 1.0;\ 2.5;\ 0.0;\ 2.0;\ -2.5;\ -0.5; \\ \}. \end{cases}$$

where: $HS^{(1,1)}_{1,1}(L)$ is the final low-frequency value after applying the Haar wavelet to the difference mini-segment $I'^{(1,1)}_{1,1}$; $HD^{(1,1)}_{1,1}$ is a set of high-frequency values after applying the Haar wavelet to the difference mini-segment $I'^{(1,1)}_{1,1}$.

The values obtained after applying the Haar wavelet to the difference mini-segments from the segment $I^{(1,1)}$ are displayed on Fig. 4.

Figure 4 shows:

- $I'^{(1,1)}_{1,1}$, $I'^{(1,1)}_{1,2}$, $I'^{(1,1)}_{2,1}$, $I'^{(1,1)}_{2,2}$ are difference mini-segments are formed from the segment $I^{(1,1)}$;
- $HD^{(1,1)}_{1,1}$ is received high-frequency values group after applying the Haar wavelet to the difference mini-segment $I'^{(1,1)}_{1,1}$;
- $HD^{(1,1)}_{1,2}$ is received high-frequency values group after applying the Haar wavelet to the difference mini-segment $I'^{(1,1)}_{1,2}$;
- $HD^{(1,1)}_{2,1}$ is received high-frequency values group after applying the Haar wavelet to the difference mini-segment $I'^{(1,1)}_{2,1}$;
- $HD^{(1,1)}_{2,2}$ is received high-frequency values group after applying the Haar wavelet to the difference mini-segment $I'^{(1,1)}_{2,2}$;
- $HS^{(1,1)}_{1,1}(L)$ is received low-frequency value after applying the Haar wavelet to the difference mini-segment $I'^{(1,1)}_{1,1}$;
- $HS^{(1,1)}_{1,2}(L)$ is received low-frequency value after applying the Haar wavelet to the difference mini-segment $I'^{(1,1)}_{1,2}$;
- $HS^{(1,1)}_{2,1}(L)$ is received low-frequency value after applying the Haar wavelet to the difference mini-segment $I'^{(1,1)}_{2,1}$;
- $HS^{(1,1)}_{2,2}(L)$ is received low-frequency value after applying the Haar wavelet to the difference mini-segment $I'^{(1,1)}_{2,2}$.

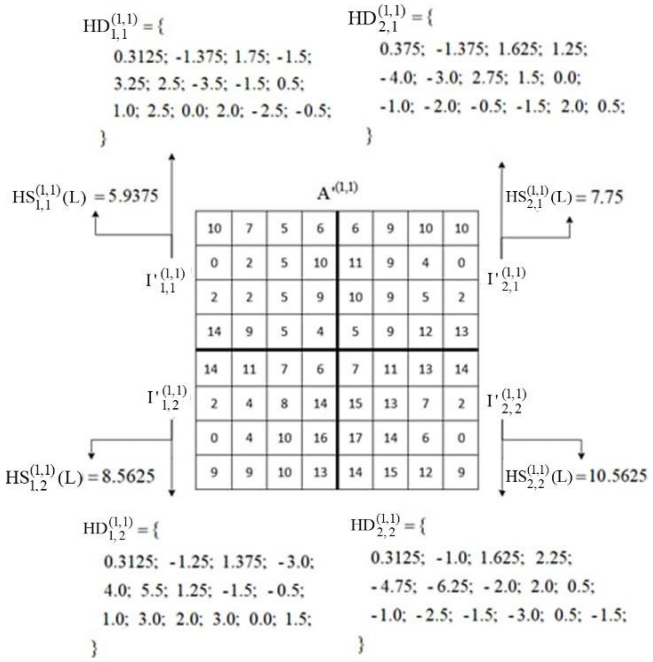

Fig. 4. Scheme of applying the Haar wavelet to the difference segment

Let's consider an example of forming a set of low-frequency values $HS^{(1,1)}$ for the segment $I^{(1,1)}$ from Fig. 3. On the Fig. 5 the diagram of the formation $HS^{(1,1)}$ based on the difference segment $I'^{(1,1)}$ is shown. $HS^{(1,1)}$ is formed from each low-frequency value obtained from the corresponding mini-segment, within the segment $I'^{(1,1)}$.

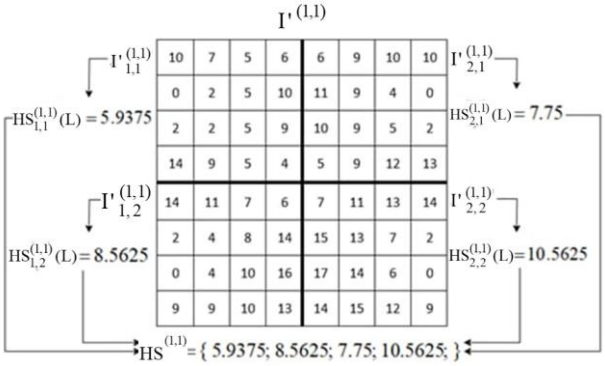

Fig. 5. Scheme of a group of low-frequency values formation

A group of low frequencies is formed:

$$HS^{(1,1)} = \{5.9375; 8.5625; 7.75; 10.5625\} \tag{13}$$

Let's apply spectral group coding to it. The calculation of the code $GC(HS^{(1,1)})$ for low-frequency values $HS^{(1,1)}$ from the segment $I^{(1,1)}$ will look like this:

$$\beta = 10.5625;$$

$$\begin{aligned} &GC(HS^{(1,1)}) = \\ &= floor(5.9375)\cdot floor(10.5625)^3 + floor(8.5625)\cdot \\ &\cdot floor(10.5625)^2 + floor(7.75)\cdot floor(10.5625)^1 + \\ &+ floor(10.5625)\cdot floor(10.5625)^0 = \\ &= 5\cdot 10^3 + 8\cdot 10^2 + 7\cdot 10^1 + 10\cdot 1 = 5880 \end{aligned} \quad (14)$$

On the next figure (Fig. 6) coding is depicted in a schematic way.

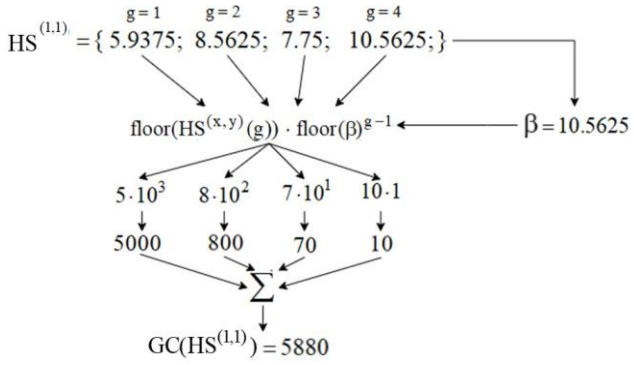

Fig. 6. The scheme of formation of a spectral group code of the low-frequency values group

Let's apply a similar coding formula for high frequencies, formula (7). To groups of high-frequency values $HD_{1,1}^{(1,1)}$, $HD_{1,2}^{(1,1)}$, $HD_{2,1}^{(1,1)}$, $HD_{2,2}^{(1,1)}$ from the example Fig. 6. The following codes are received:

$$GC(HD_{1,1}^{(1,1)}) = 2\,541\,723;\ GC(HD_{1,2}^{(1,1)}) = 1\,660\,630\,326;$$

$$GC(HD_{2,1}^{(1,1)}) = 93\,210\,136;\ GC(HD_{2,2}^{(1,1)}) = 16\,269\,331\,141$$

As a result of coding a segment $I^{(1,1)}$ can be represented as five code values: $GC(HS^{(1,1)})$, $GC(HD_{1,1}^{(1,1)})$, $GC(HD_{1,2}^{(1,1)})$, $GC(HD_{2,1}^{(1,1)})$, $GC(HD_{2,2}^{(1,1)})$.

3. Conducting a comparative evaluation of spectral data group coding with modern analogues

To objectively assess the efficiency of the proposed spectral-wave group coding method, a series of controlled experiments was conducted using representative datasets and standardized computational conditions. Before presenting the comparative results, there is a description of the datasets, execution environment, and software tools employed in the study. The inclusion of these details ensures that the experimental procedure is fully reproducible and transparent.

The evaluation involved two datasets selected to highlight different aspects of method performance. For comparison with the PNG lossless compression method, a subset of the Open Turbulent Image Set (OTIS) was used. This dataset consists of 8-bit monochrome grayscale images captured under turbulent conditions, exhibiting diverse structural patterns and textural variability. Although OTIS does not contain infrared imagery, its heterogeneous spatial properties make it suitable for analyzing bit-volume behavior under lossless compression scenarios. The resolutions of OTIS subset images range from 112×112 to 520×520 pixels, thereby covering a broad variety of spatial complexities.

A dataset of more than 100 infrared images was prepared for comparison with the JPEG2000 coding format. Each image is a 16-bit grayscale frame with a resolution of 128×128 pixels. The dataset spans multiple semantic configurations, including homogeneous backgrounds, moderately structured scenes, and high-clutter thermal environments containing multiple objects of interest. The radiometric and noise characteristics of this dataset are representative of modern uncooled thermal sensors. The type of imagery is comparable to that produced by commercially available infrared cameras such as the FLIR Tau 2, FLIR A655sc, or Seek Thermal CompactPRO, which typically output 14–16-bit thermal frames with similar dynamic ranges and contrast properties.

Owing to the computational structure of the proposed method – which relies primarily on integer differencing, Haar wavelet transforms, and low-complexity spectral-group arithmetic – real-time processing is also feasible on embedded platforms commonly used in onboard systems. Representative examples include ARM Cortex-A72/A78 processors, NVIDIA Jetson Nano/Xavier/Orin modules, and Qualcomm mobile system-on-chips. This makes the proposed coding approach compatible with practical constraints encountered in autonomous airborne, ground, or robotic platforms.

The implementation of the coding method was developed in Kotlin Multiplatform (KMP), enabling deployment across Linux, Windows, macOS, JVM-based systems, Android, and iOS environments. Matrix and numerical operations required for block transformations and frequency computations were executed using the Multik numerical library. Experimental analyses, baseline comparisons, and visualization procedures were carried out in Python using NumPy for numerical evaluation and Matplotlib for rendering plots and diagrams. All components of the experimental pipeline operate deterministically, ensuring that the reported results can be exactly replicated under the same conditions.

Let's examine the effectiveness of the developed method for group coding of data in the spectral-wave space. The effectiveness of the encoding will be evaluated based on the bit volume of the encoded data. Where the encoded data represent the obtained codes for each spectral group, specifically the values:

$$\left\{ \begin{array}{l} GC(HS^{(x,y)}), \\ GC(HD_{1,1}^{(x,y)}),\ GC(HD_{2,1}^{(x,y)}), \\ GC(HD_{1,2}^{(x,y)}),\ GC(HD_{2,2}^{(x,y)}) \end{array} \right\} \quad (15)$$

To calculate the bit volume of each individual code, we will use the following formula:

$$bits(c) = ceil(\log_2 c) \quad (16)$$

where: $bits(c)$ is a bits quantity for a value c; c is the value of the code whose bit volume is obtained; ceil is a rounding to the next whole value. For example $ceil(3.1) = 4$.

Let's apply the formula (16) for code values (15) and thus determine the bit volume of the segment $I^{(x,y)}$:

$$\begin{aligned} &bits(GC(I^{(x,y)})) = \\ &= bits(GC(HS^{(x,y)})) + bits(GC(HD_{1,1}^{(x,y)})) + \\ &+ bits(GC(HD_{2,1}^{(x,y)})) + bits(GC(HD_{1,2}^{(x,y)})) + \\ &+ bits(GC(HD_{2,2}^{(x,y)})) \end{aligned} \quad (17)$$

In order to determine the bit volume for the entire image $I^{(X,Y)}$ it is necessary to calculate the sum of bit volumes for each segment $I^{(x,y)}$, namely:

$$bits(GC(I^{(X,Y)}) = \sum bits(GC(I^{(x,y)})) \quad (18)$$

Let's compare the evaluation of the bit volume with the widely used PNG codec, which represents lossless compression. For that let's use images dataset Open Turbulent Image Set (OTIS). It contains monochrome PNG images with different levels of informativeness. The results of bit volume estimation are presented on the Fig. 7.

After analyzing the given diagram, we can draw a conclusion: images encoded using the developed group coding method in the spectral-wave space have an average bit volume of 37% less than images encoded using the PNG method.

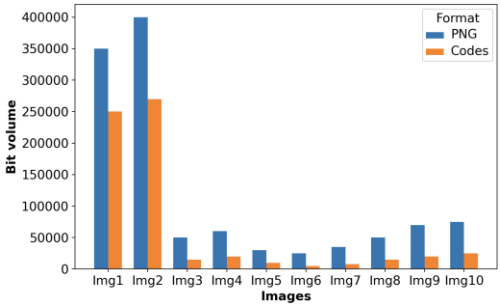

Fig. 7. Diagram of the dependence of bit volume of PNG and code values

Let's compare the coding efficiency of the developed spectral-group coding method (SGC) with the existing coding method (EMC). EMC is based on the application of Haar wavelet and Huffman coding, which is the codec used in the modern JPEG 2000 format. For this let's use a set of 16-bit images Img1_16 ... Img5_16. There are images with varying degrees of saturation and structural and visual features.

Figure 8 presents the compression ratio indicators of SGC and EMC for the corresponding images.

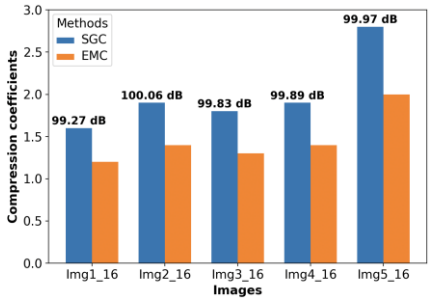

Fig. 8. Diagram of the dependence compression ratio of the developed SGC and EMC coding method for 16-bit images

All comparative assessments were made with the same preset configurations. Both approaches were applied with a minimum level of compression and have the same PSNR values, which are displayed on the Fig. 8. It can be noted that the developed method of spectral-group coding has a compression ratio that is 25% higher than the existing approach, while maintaining the same PSNR values.

Table 2 presents a comparison of the compression coefficient deviation for SGC and EMC at minimum compression level parameters, which correspond to maximum quality.

Table 2. Compression coefficient deviation for SGC and EMC with minimum compression level (maximum quality)

Method	Average	Standard deviation (unbiased)	Confidence interval
SGC	2.01	0.464	1.91 – 2.09
EMC	1.46	0.313	1.40 – 1.52

Additionally, experiments were conducted using the developed SGC method on 16-bit images at various compression levels. Figure 9 presents the rate–distortion diagram, which shows the dynamics of decrease in PSNR corresponding to the compression coefficients.

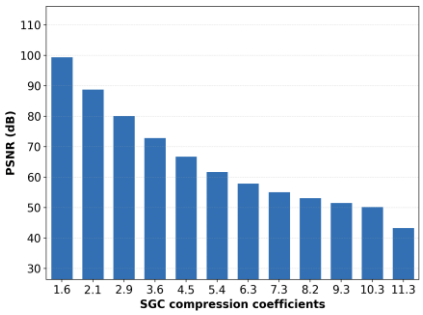

Fig. 9. Diagram of the dependence SGC compression coefficients and PSNR on 16 bit images

The contribution of the differential-space transformation to the overall efficiency of the proposed spectral-group coding method was evaluated through an ablation experiment in which this step was explicitly removed while keeping all other components unchanged. The results, summarized in Table 3, show that across test images the compression coefficient decreases consistently when differential conversion is omitted. For the full SGC pipeline, the average compression coefficients is 2.01, whereas the variant without differential space achieves only 1.62 in average. The use of differential-space transformation provides a 23% improvement in compression efficiency, demonstrating that reduction of the local dynamic range prior to wavelet analysis plays a critical role in enabling more compact spectral-group representations. This confirms that the differential step is an essential component of the method's overall performance.

Table 3. SGC without differential space ablation experiment

Image	SGC compression coefficient	Without differential space compression coefficient
Img1_16	1.6	1.45
Img2_16	1.9	1.62
Img3_16	1.8	1.53
Img4_16	1.9	1.69
Img5_16	2.8	1.81

Average execution metrics are presented in Table 4. These include encoding time, decoding time, and encoding and decoding memory consumption. Execution for measurements was conducted on the chip Apple M3 Max.

It is notable that SGC demonstrates better execution efficiency than JPEG 2000. This is expected, as JPEG 2000 has higher computational complexity due to bit-plane encoding and complex CABAC entropy coding.

At the same time, PNG exhibits significantly better execution metrics than SGC because of its simplicity. However, PNG is not as effective at reducing bit volume, as shown in Fig. 7.

Table 4. Execution metrics for SGC, JPEG 2000 and PNG

Method	SGC	JPEG 2000	PNG
Avg. Encoding time (ms)	9.45	9.84	3.9
Avg. Decoding time (ms)	3.63	3.82	0.66
Avg. Encoding Memory (kb)	258.81	287.56	69.78
Avg. Decoding Memory (kb)	867.59	1032.84	22.28

For practical deployment in onboard systems, the proposed method is compatible with a wide range of embedded hardware platforms that provide sufficient compute throughput and low-latency video processing. Recommended solutions include NVIDIA Jetson Xavier and Orin modules, Rockchip RK3588, and Qualcomm Snapdragon-class SoCs, all of which offer hardware-accelerated video pipelines and the computational headroom required for real-time spectral and wavelet operations. At the same time, several limitations should be acknowledged. In scenarios with highly non-stationary scenes or rapid thermal fluctuations, local homogeneity assumptions may degrade, reducing the efficiency of differential and spectral grouping.

Additionally, the achievable real-time throughput depends on link bandwidth, which may constrain performance in low-rate or high-latency communication channels. Despite these limitations, the method remains suitable for most onboard IR-streaming applications where low-complexity compression and predictable processing time are required.

The overview of the experimental stage that includes information about datasets, baselines, metrics, gains, and timing is presented in the Table 5.

Table 5. Experimental overview

Datasets	OTIS (8-bit, 112×112–520×520): - grayscale turbulent scenes; - used for lossless comparison with PNG.
	Custom IR Dataset (16-bit, 128×128, N>100): - thermal frames with varying semantic complexity; - used for comparisons with EMC and ablations.
Baselines	PNG (lossless): reference for bit-volume comparison on OTIS.
	EMC: reference for compression ratio and rate–distortion tests on 16-bit IR images.
	Ablation variants: SGC without differential space.
Evaluation Metrics	Rate metrics: bit volume, compression ratio.
	Distortion metrics: PSNR.
	Statistical metrics: mean ± 95%.
	Complexity metrics: encoding/decoding time, memory footprint
Main Gains Achieved	PNG comparison: 37% reduction in bit volume.
	EMC comparison: 25% higher compression ratio at equal PSNR.
	Ablation (no differential space): 23% lower compression efficiency.
Timing and Hardware	Workstation: chip Apple M3 Max. Full SGC pipeline: 8-15 ms per 128×128 frame.
	Embedded: NVIDIA Jetson Xavier and Orin modules, Rockchip RK3588, Qualcomm Snapdragon-class SoCs. Real-time feasibility (≤30 fps).
Implementation	Core codec: Kotlin Multiplatform, Multik.
	Analysis: Python (NumPy, Matplotlib).

Future research may explore adaptive block-size selection to better match local scene structure and further improve compression efficiency in heterogeneous regions. An additional direction involves evaluating alternative wavelet bases that may provide improved energy compaction for specific infrared textures. The method could also be extended with lightweight learned post-filters to enhance reconstruction quality without increasing the core coding complexity. Finally, integrating region-of-interest (ROI) priority modes would allow allocating higher fidelity to semantically important areas, enabling more efficient use of bandwidth in demanding real-time applications.

4. Conclusions

1. A method for group coding of infrared images in the spectral-wave space has been developed. The method is based on:
   1) hierarchical decomposition of infrared images into segments and mini-segments for the localization of homogeneous areas;
   2) transformation of information into the difference space to reduce the dynamic range of values while considering correlation dependencies;
   3) transformation of the spatial domain information into the spectral-wave domain using the Haar wavelet;
   4) grouping high and low frequencies to account for their structural patterns.;
   5) application of spectral-group coding to the formed groups for their effective bit representation..
2. The obtained results of experimental comparisons of the developed coding method confirm its advantages over current solutions.

Compared to the current lossless compression method PNG, the spectral-group coding method allows for the encoded image to be represented with a 37% smaller bit volume (Fig. 7).

When comparing the coding method with the JPEG 2000 format, which includes the use of the Haar wavelet and Huffman coding, the developed coding method achieves a compression ratio that is 25% higher (Fig. 8). The comparison was conducted at the same PSNR values.

Scientific novelty.

Developed the positional coding method in differential wave space for encoding segments of infrared image. A key feature of the method is group coding in the spectral-wave space based on the consideration of local correlation dependencies. As a result, groups of spectral values are represented in the form of corresponding codes. This allows for the enhancement of quality characteristics in providing intelligent services for the transmission of infrared images in applied tasks using onboard systems.

References

[1] Barannik, D., & Barannik, V. (2022). Steganographic Coding Technology for Hiding Information in Infocommunication Systems of Critical Infrastructure. *2022 IEEE 4th International Conference on Advanced Trends in Information Theory (ATIT)*, 88–91. https://doi.org/10.1109/ATIT58178.2022.10024185

[2] Barannik, V., Shulgin, S., Barannik, N., & Barannik, V. (2022). Method of Coding Subbands of Non-Homogeneous Spectrum of Video Segments in Uneven Diagonal Space. *2022 IEEE 4th International Conference on Advanced Trends in Information Theory (ATIT)*, 72–75. https://doi.org/10.1109/ATIT58178.2022.10024236

[3] Barannik, V., Sidchenko, S., Barannik, N., & Khimenko, A. (2021). The method of masking overhead compaction in video compression systems. *Radioelectronic and Computer Systems*, (2), 51–63. https://doi.org/10.32620/reks.2021.2.05

[4] Descampe, A., Richter, T., Ebrahimi, T., Foessel, S., Keinert, J., Bruylants, T., Pellegrin, P., Buysschaert, C., & Rouvroy, G. (2021). JPEG XS – A New Standard for Visually Lossless Low-Latency Lightweight Image Coding. *Proceedings of the IEEE*, *109*(9), 1559–1577. https://doi.org/10.1109/JPROC.2021.3080916

[5] Dua, Y., Kumar, V., & Singh, R. S. (2020). Comprehensive review of hyperspectral image compression algorithms. *Optical Engineering*, *59*(09). https://doi.org/10.1117/1.OE.59.9.090902

[6] Fauziah, Lantana, D. A., Nurhayati, Sholihati, I. D., Komala Sari, R. T., & Hendrik, B. (2023). An Extensive Analysis of Digital Image Compression Techniques Using Different Image Files and Color Formats. *International Journal on Advanced Science, Engineering and Information Technology*, *13*(5), 1971–1977. https://doi.org/10.18517/ijaseit.13.5.19319

[7] Hazowary, P., Dutta, S. K., & Subadar, R. (2022). A Comparison of Image Compression Techniques Over Wireless Fading Channel. In H. K. D. Sarma, V. E. Balas, B. Bhuyan, & N. Dutta (Eds), *Contemporary Issues in Communication, Cloud and Big Data Analytics* (Vol. 281, pp. 241–249). Springer Singapore. https://doi.org/10.1007/978-981-16-4244-9_19

[8] Hu, Y., Yang, W., Ma, Z., & Liu, J. (2021). Learning End-to-End Lossy Image Compression: A Benchmark. *IEEE Transactions on Pattern Analysis and Machine Intelligence*, 1–1. https://doi.org/10.1109/TPAMI.2021.3065339

[9] Hua, K.-L., Trang, H. T., Srinivasan, K., Chen, Y.-Y., Chen, C.-H., Sharma, V., & Zomaya, A. Y. (2019). Reduction of Artefacts in JPEG-XR Compressed Images. *Sensors*, *19*(5), 1214. https://doi.org/10.3390/s19051214

[10] Iwahashi, M., & Kiy, H. (2013). Non Separable Two Dimensional Discrete Wavelet Transform for Image Signals. In Dr. A. Al-Asmari (Ed.), *Discrete Wavelet Transforms – A Compendium of New Approaches and Recent Applications*. InTech. https://doi.org/10.5772/51199

[11] Jamil, S. (2024). Review of Image Quality Assessment Methods for Compressed Images. *Journal of Imaging*, *10*(5), 113. https://doi.org/10.3390/jimaging10050113

[12] Lee, S., Jeong, J.-B., & Ryu, E.-S. (2023). Entropy-Constrained Implicit Neural Representations for Deep Image Compression. *IEEE Signal Processing Letters*, *30*, 663–667. https://doi.org/10.1109/LSP.2023.3279780

[13] Lieberman, K., Diffenderfer, J., Godfrey, C., & Kailkhura, B. (2023). Neural Image Compression: Generalization, Robustness, and Spectral Biases. *37th Conference on Neural Information Processing Systems (NeurIPS)*, 8343. https://openreview.net/forum?id=FxRfAIj4s2

[14] Lungisani, B. A., Lebekwe, C. K., Zungeru, A. M., & Yahya, A. (2022). Image Compression Techniques in Wireless Sensor Networks: A Survey and Comparison. *IEEE Access*, *10*, 82511–82530. https://doi.org/10.1109/ACCESS.2022.3195891

[15] Ma, H., Liu, D., Yan, N., Li, H., & Wu, F. (2022). End-to-End Optimized Versatile Image Compression With Wavelet-Like Transform. *IEEE Transactions on Pattern Analysis and Machine Intelligence*, *44*(3), 1247–1263. https://doi.org/10.1109/TPAMI.2020.3026003

[16] Mishra, D., Singh, S. K., & Singh, R. K. (2021). Wavelet-Based Deep Auto Encoder-Decoder (WDAED)-Based Image Compression. *IEEE Transactions on Circuits and Systems for Video Technology*, *31*(4), 1452–1462. https://doi.org/10.1109/TCSVT.2020.3010627

[17] Rahman, Md. A., Hamada, M., & Shin, J. (2021). The Impact of State-of-the-Art Techniques for Lossless Still Image Compression. *Electronics*, *10*(3), 360. https://doi.org/10.3390/electronics10030360
[18] Ranjan, R., & Kumar, P. (2023). An Improved Image Compression Algorithm Using 2D DWT and PCA with Canonical Huffman Encoding. *Entropy*, *25*(10), 1382. https://doi.org/10.3390/e25101382
[19] Rasheed, M. H., Salih, O. M., Siddeq, M. M., & Rodrigues, M. A. (2020). Image compression based on 2D Discrete Fourier Transform and matrix minimization algorithm. *Array*, *6*, 100024. https://doi.org/10.1016/j.array.2020.100024
[20] Richter, T., Fobel, S., Descampe, A., & Rouvroy, G. (2021). Bayer CFA Pattern Compression With JPEG XS. *IEEE Transactions on Image Processing*, *30*, 6557–6569. https://doi.org/10.1109/TIP.2021.3095421
[21] Shihab, H. S. (2023). Image Compression Techniques on-Board Small Satellites. *Iraqi Journal of Science*, 1518–1534. https://doi.org/10.24996/ijs.2023.64.3.40
[22] Siddeq, M. M., & Rodrigues, M. A. (2020). A Novel Method for Image and Video Compression Based on Two-Level DCT with Hexadata Coding. *Sensing and Imaging*, *21*(1), 36. https://doi.org/10.1007/s11220-020-00302-6
[23] Thomas, S., Krishna, A., Govind, S., & Sahu, A. K. (2025). A novel image compression method using wavelet coefficients and Huffman coding. *Journal of Engineering Research*, *13*(1), 361–370. https://doi.org/10.1016/j.jer.2023.08.015
[24] Ungureanu, V.-I., Negirla, P., & Korodi, A. (2024). Image-Compression Techniques: Classical and "Region-of-Interest-Based" Approaches Presented in Recent Papers. *Sensors*, *24*(3), 791. https://doi.org/10.3390/s24030791
[25] Uthayakumar, J., Elhoseny, M., & Shankar, K. (2020). Highly Reliable and Low-Complexity Image Compression Scheme Using Neighborhood Correlation Sequence Algorithm in WSN. *IEEE Transactions on Reliability*, *69*(4), 1398–1423. https://doi.org/10.1109/TR.2020.2972567
[26] Valente, J., António, J., Mora, C., & Jardim, S. (2023). Developments in Image Processing Using Deep Learning and Reinforcement Learning. *Journal of Imaging*, *9*(10), 207. https://doi.org/10.3390/jimaging9100207
[27] Yousif, R. I., & Salman, N. H. (2021a). Image Compression Based on Arithmetic Coding Algorithm. *Iraqi Journal of Science*, 329–334. https://doi.org/10.24996/ijs.2021.62.1.31

Prof. Volodymyr Barannik
e-mail: vvbar.off@gmail.com

Doctor of Technical Sciences, professor at Department of Artificial Intelligence and Software V. N. Karazin Kharkiv National University.
Scientific interests: information security, image processing, information coding.

http://orcid.org/0000-0002-2848-4524

M.Sc. Mykola Dihtiar
e-mail: nikdeg1960@gmail.com

Senior lecturer of the Department of Radioelectronic Equipment of Aircraft, Ivan Kozhedub Kharkiv National Air Force University.
Scientific interests: information security.

https://orcid.org/0000-0001-9208-7593

M.Sc. Anatolii Berchanov
e-mail: tberchanov@gmail.com

Ph.D. student at V.N. Karazin Kharkiv National University, Ukraine.
Scientific interests: information technology, image processing, information coding.

https://orcid.org/0009-0004-4301-6384

M.Sc. Mykhailo Osovytskyi
e-mail: samsung.myhailo@gmail.com

Senior lecturer of the Department of Aerodynamics and Flight Dynamics, Ivan Kozhedub Kharkiv National Air Force University.
Scientific interests: image processing, information coding.

http://orcid.org/0009-0006-5944-3334

M.Sc. Valeriy Barannik
e-mail: valera462000@gmail.com

Ph.D. student at Department of Information and Network Engineering, Kharkov National University of Radio Electronics.
Scientific interests: systems, technologies of transformation, encoding, defense and information transfer, semantic processing of images.

http://orcid.org/0000-0003-3516-5553

Ph.D. Andrii Sushko
e-mail: sushko74andrey@gmail.com

Deputy Head of the Department of Flight Operations and Combat Use of Aircraft, Ivan Kozhedub Kharkiv National Air Force University.
Scientific interests: information security.

http://orcid.org/0000-0002-1387-5733

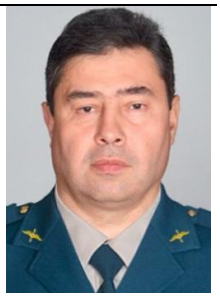

Ph.D. Dmytro Uzlov
e-mail: dmytro.uzlov@karazin.ua

Candidate of Technical Sciences. Director of the Educational and Research Institute of Computer Sciences and Artificial Intelligence V.N. Karazin Kharkiv National University.
Scientific interests: Data Analysis, Artificial Intelligence, NLP for criminal intelligence, digital forensics knowledge representation, computational criminology, knowledge graphs for crime analysis, semantic web in law enforcement, computer vision.

https://orcid.org/0000-0003-3308-424X

Ph.D. Yurii Babenko
e-mail: yurii.babenko@knu.ua

Assistant professor in the Department of Cybersecurity and Information Protection, Taras Shevchenko National University of Kyiv, Kyiv, Ukraine.
Scientific interests: information security.

http://orcid.org/0000-0002-8115-3329